



LAWRENCE
LIVERMORE
NATIONAL
LABORATORY

Regularization of Arbitrary Lagrangian-Eulerian Hydrodynamics on Unstructured Grids

A. W. Cook, M. S. Ulitsky, D. S. Miller

November 18, 2011

International Journal of Computational Fluid Dynamics

Disclaimer

This document was prepared as an account of work sponsored by an agency of the United States government. Neither the United States government nor Lawrence Livermore National Security, LLC, nor any of their employees makes any warranty, expressed or implied, or assumes any legal liability or responsibility for the accuracy, completeness, or usefulness of any information, apparatus, product, or process disclosed, or represents that its use would not infringe privately owned rights. Reference herein to any specific commercial product, process, or service by trade name, trademark, manufacturer, or otherwise does not necessarily constitute or imply its endorsement, recommendation, or favoring by the United States government or Lawrence Livermore National Security, LLC. The views and opinions of authors expressed herein do not necessarily state or reflect those of the United States government or Lawrence Livermore National Security, LLC, and shall not be used for advertising or product endorsement purposes.

Regularization of Arbitrary Lagrangian-Eulerian Hydrodynamics on Unstructured Grids

Andrew W. Cook, Mark S. Ulitsky and Douglas S. Miller

Lawrence Livermore National Laboratory

Abstract

An artificial viscosity, originally designed for Eulerian schemes, is adapted for use in arbitrary Lagrangian-Eulerian simulations. Changes to the Eulerian model, dubbed “hyperviscosity”, are discussed, which enable it to work within a Lagrangian framework. New features include a velocity-weighted grid scale and a generalized filtering procedure, applicable to either structured or unstructured grids. The model employs an artificial shear viscosity for treating small-scale vorticity and an artificial bulk viscosity for shock capturing. The model is based on the Navier-Stokes form of the viscous stress tensor, including the diagonal rate-of-expansion tensor. A second-order version of the model is presented, in which Laplacian operators act on the velocity divergence and the grid-weighted strain-rate magnitude to ensure that the velocity field remains smooth at the grid scale. The new model is compared to a previously published Lagrangian artificial viscosity on a variety of test problems.

Keywords: ALE, hyperviscosity, artificial viscosity, shocks, turbulence

1. Introduction

For the past six decades, numerical simulations of shocks and turbulence have been performed by time-marching the discretized Euler equations. The inherent instability of these calculations motivated von Neumann and Richtmyer [1] early on to introduce an artificial viscosity term into the equations in order to help regularize the solutions. Since the 1950s, numerous artificial damping terms have been proposed for simulating both shocks and turbulence [2, 3, 4, 5, 6, 7, 8, 9]. The multiplicity of artificial viscosity models in use today reflects the problem-specific nature of their formulations.

The proper (frame-independent) form of the viscous stress tensor was found by Claude-Louis Navier [10] and George Gabriel Stokes [11]. Stokes, in particular, reasoned that viscous forces, resulting from relative motion between fluid elements, are a function of the Jacobian of the velocity field. The Jacobian matrix can be decomposed into symmetric and antisymmetric parts, independent of the coordinate system. The antisymmetric part represents rigid rotation (no relative motion of fluid elements) and thus has no associated viscous force. The symmetric part (the rate-of-strain tensor) can be written in a frame-independent manner for an isotropic fluid as the sum of a constant rate-of-expansion tensor and a traceless symmetric rate-of-shear tensor. The most general linear relationship between the stress tensor and the rate-of-strain tensor is then a linear combination of these two tensors. The coefficient of the rate-of-expansion tensor is called “bulk viscosity” and the rate-of-strain coefficient is called “shear viscosity”. Stokes hypothesized that the trace of the total stress tensor ought to vanish and thus he assigned a relationship between the two viscosity coefficients to make the bulk viscosity zero.

Our purpose is to demonstrate that many problems with artificial viscosity models can be solved by returning to the Navier-Stokes form of the viscous stress tensor and retaining the bulk viscosity term. By modifying only the coefficients of the frame-independent rate-of-strain and rate-of-expansion tensors, both shocks and turbulence can be captured in a wide range of problems without adjusting coefficients or introducing limiters, switches or other ad hoc fixes. We are particularly motivated by astrophysical and Inertial Confinement Fusion (ICF) applications, where both shocks and turbulence play important roles.

The organization of this paper is as follows. In Section 2 we present the governing hydrodynamic equations in an arbitrary Lagrangian-Eulerian (ALE) frame of reference. In Section 3 we discuss our Navier-Stokes-based hyperviscosity model and briefly describe the well-known artificial viscosity model of Caramana, Shashkov and Whalen (CSW) [12]. In Section 4 we compare our hyperviscosity model to the CSW model on a variety of test problems. Finally, we present our conclusions in Section 5.

2. Governing Equations

The transport equations for mass, momentum and energy of a nonconductive fluid are:

$$\frac{D\rho}{Dt} = -\rho(\nabla \cdot \mathbf{u}) = -\rho \frac{\partial u_i}{\partial x_i} , \quad (1)$$

$$\rho \frac{D\mathbf{u}}{Dt} = \nabla \cdot (-p\mathbf{I} + \mathbf{Q}) = -\frac{\partial p}{\partial x_i} + \frac{\partial Q_{ij}}{\partial x_j} , \quad (2)$$

$$\rho \frac{De}{Dt} = -p(\nabla \cdot \mathbf{u}) + \mathbf{Q} : \nabla \mathbf{u} = -p \frac{\partial u_i}{\partial x_i} + Q_{ij} \frac{\partial u_i}{\partial x_j} , \quad (3)$$

where ρ is density, \mathbf{u} is material velocity, p is pressure, \mathbf{I} is the unit tensor, \mathbf{Q} is the viscous stress tensor and e is thermal energy. The material derivatives of a scalar (ϕ) and vector (ϕ) on an ALE mesh are given by:

$$\frac{D\phi}{Dt} = \frac{\partial \phi}{\partial t} + (\mathbf{u} - \hat{\mathbf{u}}) \cdot \nabla \phi = \frac{\partial \phi}{\partial t} + (u_i - \hat{u}_i) \frac{\partial \phi}{\partial x_i} , \quad (4)$$

$$\frac{D\phi}{Dt} = \frac{\partial \phi}{\partial t} + [(\mathbf{u} - \hat{\mathbf{u}}) \cdot \nabla] \phi = \frac{\partial \phi_i}{\partial t} + (u_j - \hat{u}_j) \frac{\partial \phi_i}{\partial x_j} , \quad (5)$$

where $\hat{\mathbf{u}}$ is the grid-node velocity and the partial time-derivatives are evaluated holding nodal coordinates fixed. For Newtonian fluids, the viscous stress tensor is

$$\mathbf{Q} = \mu \left[2\mathbf{S} - \frac{2}{3}(\nabla \cdot \mathbf{u})\mathbf{I} \right] + \beta(\nabla \cdot \mathbf{u})\mathbf{I} = \mu \left[2S_{ij} - \frac{2}{3} \frac{\partial u_k}{\partial x_k} \delta_{ij} \right] + \beta \frac{\partial u_k}{\partial x_k} \delta_{ij} , \quad (6)$$

where μ is the shear viscosity, β is the bulk viscosity and \mathbf{S} is the symmetric strain-rate tensor,

$$\mathbf{S} = \frac{1}{2} [\nabla \mathbf{u} + (\nabla \mathbf{u})^\dagger] = S_{ij} = \frac{1}{2} \left(\frac{\partial u_i}{\partial x_j} + \frac{\partial u_j}{\partial x_i} \right) . \quad (7)$$

For an ideal gamma-law gas,

$$p = (\gamma - 1)\rho e , \quad (8)$$

where $\gamma = c_p/c_v$ is the ratio of specific heats (adiabatic index).

Equations (1)-(8) adequately describe a wide variety of flow phenomena, including shocks, expansions, instabilities, turbulence, vortex dynamics,

boundary layers, sound waves, etc. They constitute a closed set of equations which, when combined with a complete set of initial/boundary conditions, comprise a well-posed system. In many cases however, they admit solutions that contain scales of motion too small to be resolved on any affordable mesh; hence, the viscous terms must be modified to provide a grid-scale cut-off.

3. Artificial Viscosity

3.1. Hyperviscosity

A practice that has proven very effective in Eulerian calculations at removing subgrid-scale features, while minimally affecting grid-scale physics, is to add high-order grid-dependent components to the molecular transport coefficients, i.e., to set:

$$\mu = \mu_{\mathcal{F}} + \mu^* , \quad (9)$$

$$\beta = \beta_{\mathcal{F}} + \beta^* , \quad (10)$$

where an \mathcal{F} subscript denotes a physical fluid property and an asterisk denotes an artificial property [13, 14, 15, 16, 17, 18, 19, 20, 21, 22, 23, 24, 25]. It is often the case, in simulating high-Reynolds-number flows on coarse grids, that physical fluid properties are negligible compared to the requisite artificial properties. Therefore, in our present investigations we set $\mu_{\mathcal{F}} = \beta_{\mathcal{F}} = 0$ and limit the scope of this paper to an examination of just μ^* and β^* .

Effective functional forms of μ^* and β^* can be deduced by analogy to the scale-limiting behavior of the molecular viscosities. In a real fluid, molecules transport and exchange their momentum in such a manner as to ensure that the rate-of-strain tensor, \mathbf{S} , is smoothed at the Kolmogorov scale [26]. In a simulated fluid, where the grid scale may be much larger than the Kolmogorov scale, we can use μ^* to limit the curvature of the strain rate and hence ensure smoothness of the velocity field at this larger scale.

In high Mach number flows, bulk viscosity can have a significant influence on the structure of shockwaves. Bulk viscosity effects arise from two separate phenomena: rotational nonequilibrium (zero for monatomic gases) and finite ranges of intermolecular forces (proportional to the volume fraction actually occupied by the molecules). In a real fluid, bulk viscosity acts to ensure that shocks are spread over a few mean-free paths. In a simulated fluid, we can use β^* to spread shocks over a few grid points.

In order to capture very strong shocks, β^* must become large. This raises the question as to whether such a shock-capturing scheme might be

excessively dissipative for instabilities, turbulence or other vortical flow phenomena. A good way to answer this question (in part) is to examine the influence of bulk viscosity on the vorticity equation. The vorticity equation for viscous compressible flow is

$$\frac{\partial \boldsymbol{\omega}}{\partial t} + \nabla \times (\boldsymbol{\omega} \times \mathbf{u}) = \frac{\nabla \rho \times \nabla p}{\rho^2} + \nabla \times \left(\frac{\nabla \cdot \mathbf{Q}}{\rho} \right) , \quad (11)$$

where $\boldsymbol{\omega} \equiv \nabla \times \mathbf{u}$ is the vorticity pseudovector. The bulk viscosity term on the right-hand side of this equation is

$$\nabla \times \left\{ \frac{1}{\rho} \nabla \cdot [\beta (\nabla \cdot \mathbf{u}) \mathbf{I}] \right\} = -\frac{1}{\rho^2} \nabla \rho \times \nabla [\beta (\nabla \cdot \mathbf{u})] . \quad (12)$$

At shocks, $\nabla \rho$ aligns with $\nabla [\beta (\nabla \cdot \mathbf{u})]$; hence, even a very large bulk viscosity will have minimal effect on the vorticity field.

We have found the following second-order formulations of μ^* and β^* to provide effective grid-scale smoothing of both turbulence and shocks:

$$\mu^* = \overline{C_\mu \rho |\nabla^2 (SL^4)|} , \quad (13)$$

$$\beta^* = \overline{C_\beta \rho |\nabla^2 (\nabla \cdot \mathbf{u})| L^4} , \quad (14)$$

where $S = (\mathbf{S} : \mathbf{S})^{1/2} = (S_{ij}S_{ji})^{1/2}$ is the magnitude of the strain rate tensor, L is a velocity-weighted grid scale (to be discussed) and C_μ and C_β are empirical coefficients, which we set to:

$$C_\mu = 0.16 , \quad (15)$$

$$C_\beta = \begin{cases} 2.2 & \text{if } \nabla \cdot \mathbf{u} \leq 0 \\ 0 & \text{if } \nabla \cdot \mathbf{u} > 0 \end{cases} . \quad (16)$$

All of the problems reported herein were run with these default values of the model coefficients. For brevity, we refer to the use of (13) and (14) in (6) as the “Hyper-Q” model.

3.2. Zone Length Scale

On uniform Cartesian grids, L is simply the distance between grid nodes. On stretched grids however, L must be computed in a manner appropriate for high-aspect-ratio zones. Since the purpose of hyperviscosity is to smooth velocity gradients with respect to the grid scale, it makes sense to weight

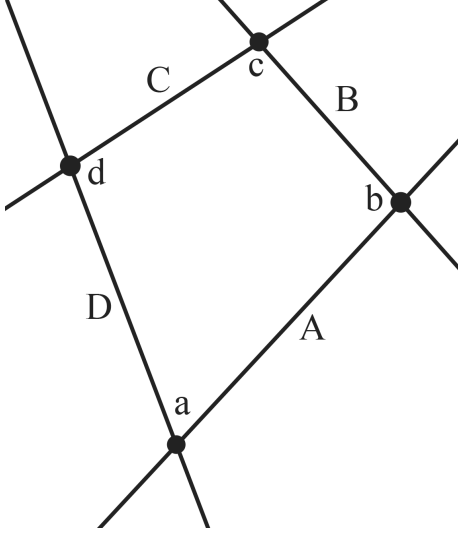


Figure 1: A grid cell with four edges: A, B, C, D and four nodes: a, b, c, d.

each cell edge by its associated velocity jump. We have found the following formula to work well in practice,

$$L = \frac{\sum_{\xi=1}^n \|\Delta \mathbf{u}\|_{\xi}}{\sum_{\xi=1}^n \|\Delta \mathbf{u}\|_{\xi} / L_{\xi} + \epsilon / \Delta t} , \quad (17)$$

where n is the number of cell edges, L_{ξ} is the length of an edge of index ξ , $\|\Delta \mathbf{u}\|_{\xi}$ is the magnitude of the corresponding velocity jump, Δt is the time step and ϵ is a tiny number, required to avoid division by zero. Figure 1 provides an illustration of a (structured or unstructured) grid cell where $n = 4$. The velocity jump associated with edge A would be computed as the difference between the a and b nodal velocities; i.e., $\|\Delta \mathbf{u}\|_A = \|\mathbf{u}_b - \mathbf{u}_a\|$. Equation (17) effectively selects the grid spacing normal to shocks, which is necessary to ensure that shock profiles remain independent (in terms of number of grid points) of their orientation with respect to the anisotropic grid [19].

3.3. Filter Operator

The absolute value operators in (13) and (14) ensure that μ^* and β^* are positive definite; however, they introduce cusps in the scalar fields. The cusps are removed by applying a smoothing operator, denoted by an overbar, which

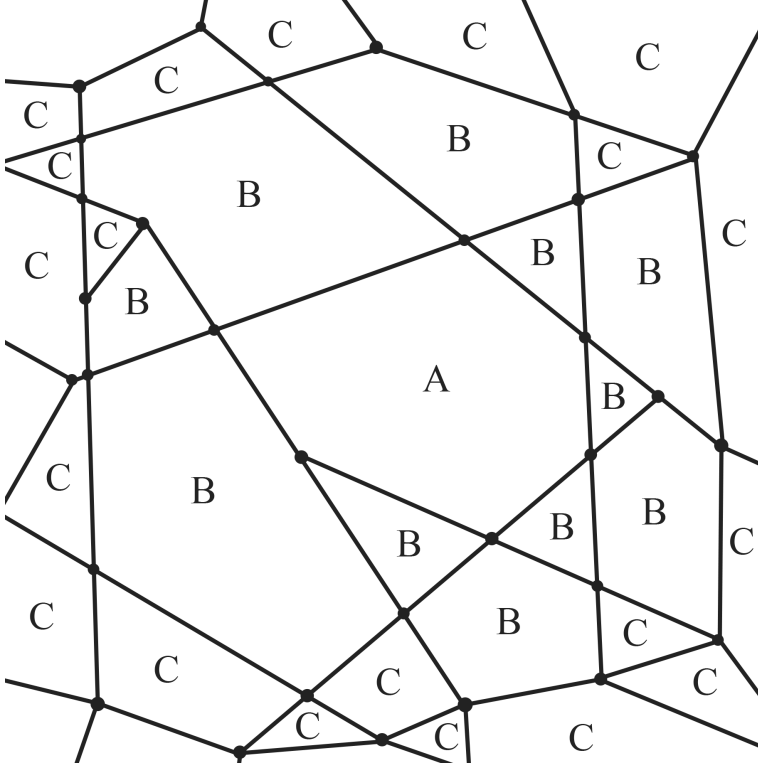


Figure 2: An unstructured mesh with central zone “A” ($\alpha = 0$), first neighbors “B” and second neighbors “C”.

consists of a local average among neighboring grid cells. The zone filter can be applied on any grid by tagging all of the zones sharing a node with the zone in question, averaging over the tagged cells, then repeating the procedure; i.e.,

$$\phi' = \frac{1}{N+1} \sum_{\alpha=0}^N \phi_{\alpha} , \quad \bar{\phi} = \frac{1}{N+1} \sum_{\alpha=0}^N \phi'_{\alpha} , \quad (18)$$

where N is the number of neighboring zones (excluding duplicates) to the zone denoted by $\alpha = 0$. For example, in Fig. 2, ϕ' for cell A would consist of an average over the A and B cells, and $\bar{\phi}$ would also include the C cells. Thus, the C and B/A cells are respectively given single and double weights in the average.

Boundaries of the computational domain are treated by excluding edge cells from the average; i.e., if any of the A, B or C cells reside on a global-

domain boundary, they are not included in the summation (and N is reduced accordingly). The boundary zones thus inherit μ^* and β^* from their inside neighbors.

3.4. Turning Off β in Expansions

The Laplacian operators in (13) and (14) impart a squared-wavenumber weighting to μ^* and β^* in Fourier space (hence the label “hyperviscosity”) [13]. It has previously been demonstrated that such a weighting for μ^* enables it to function as an effective subgrid-scale turbulence model [14]. Higher-order formulations can be employed by taking a series of Laplacians (by applying a biharmonic or polyharmonic operator) and increasing the power of L accordingly [15, 18]. These higher-order versions however, can only be computed with correspondingly high-order-accurate differencing stencils, which may be impractical on unstructured grids. The hyperviscosity terms are designed to vanish wherever the flow is sufficiently smooth with respect to the grid scale. The Laplacians serve to localize the artificial damping, effectively turning it off in regions of constant shear or uniform compression. On Eulerian grids, we have found the Laplacian(s) sufficient to automatically turn off bulk viscosity in regions of expansion. On Lagrangian grids however, where the zones inflate in regions of positive divergence (making L become large), we find it necessary to manually turn off β^* according to (16). We find it unnecessary to apply this switch to μ^* because $C_\mu \ll C_\beta$.

In (13), L^4 appears in the argument of the Laplacian operator. This has the effect of increasing artificial shear viscosity in regions of severe grid distortion. We have found that this enables some Lagrangian calculations to proceed further than they would if L^4 were outside the Laplacian. On uniform grids, it makes no difference whether L^4 appears inside or outside the Laplacian.

3.5. Viscous Stability Limit

Since μ and β can become large in the presence of strong shear or strong shocks, the time step must be restricted to obey the viscous stability limit. We employ a time-step control based on the Courant condition,

$$\Delta t_{CFL} = \sigma_{CFL} \text{MIN} \left(\frac{\Delta x_{CFL}}{c_s} \right), \quad (19)$$

where Δx_{CFL} is a geometric length scale (the minimum of one-half the minimum edge length or the minimum distance between edge centers and the

zone center, whichever is smaller), c_s is a generalized sound speed for the zone, and σ_{CFL} is the CFL number (a constant). The square of the generalized sound speed consists of a thermodynamic component evaluated at constant entropy (ψ) as well as a contribution due to the artificial viscosity. It can be expressed as:

$$c_s^2 = \left(\frac{\partial p}{\partial \rho} \right)_\psi + \frac{p_Q}{\rho} . \quad (20)$$

The pressure due to hyperviscosity is defined as:

$$p_Q \equiv \sigma_Q^2 \text{MAX}(\mu^2, \beta^2) \frac{\Delta x_{CFL}^2}{\rho L_Q^4} , \quad (21)$$

where σ_Q is a constant (set to 3.0 for all simulations herein) and L_Q is related to L and Δx_{CFL} by:

$$L_Q = \text{MAX}(L, 0.01 \Delta x_{CFL}) . \quad (22)$$

By computing c_s and Δt_{CFL} with the artificial pressure p_Q , the Courant condition is modified to include the viscous restriction.

3.6. CSW Viscosity

In order to assess the relative performance of our hyperviscosity model against a more standard artificial viscosity, we have implemented the Hyper-Q model in an ICF code at LLNL. The code solves the Euler equations in a Lagrangian reference frame using a staggered-mesh formalism and the ALE hydrodynamics algorithm of Caramana et al. [27, 28]. Forces and velocities are centered on mesh nodes, whereas density, internal energy, and pressure are centered on mesh cells. A “mimetic” scheme of finite-volume operators ensures that total energy is conserved to round-off error (see [27] for details). The Euler equations are advanced via second-order Runge-Kutta integration.

In addition to artificial viscosity, the code employs hourglass control (HGC) methods to help preserve mesh quality. The code has two HGC options: one based on the well-known Flanagan-Belytschko filtering approach [29, 30], and another based on the “corner-pressures” method, of Caramana and Shashkov [31]. The simulations presented herein were performed with the corner-pressures (HGC) scheme. In this method, Lagrangian corner masses (in 2D, a corner is the quadrilateral defined by a zone-center, a node, and the two edge-centers adjacent to the node) develop pressures independent of

the zone pressure. The corner pressures produce restoring forces that act to reduce zone distortion; hence reducing hourglass modes. A danger of this approach is the extra “stiffness” generated by the corner pressures, which can inhibit physical motions. On smooth meshes, HGC-stiffening is typically a small effect; however, it can become large if the Lagrangian grid becomes highly distorted [31].

The code has long employed the edge-centered CSW viscosity model [12] as its default artificial viscosity. For brevity, we will refer to this as the “CSW-Q” model. The strengths and weaknesses of this model have been explored by Campbell and Shashkov [32]. The CSW-Q model is formally an edge-centered tensor, defined by the velocity gradient taken along an edge of the mesh. It is based on the Kuropatenko scalar formulation, which relies on the fluid’s sound speed and adiabatic index for scaling [33, 3]. Because the velocity gradient operator has no information about velocity variations in any directions other than along cell edges, CSW-Q is strongly dependent upon the quality of the mesh. The CSW-Q model employs a limiter function, designed to switch off the viscosity for uniform compression, rigid rotation and along fronts of constant phase. For the comparisons presented in this paper, we kept the limiter on and used the CSW-recommended values of unity for both model constants (the linear and quadratic coefficients). The CSW-Q model serves in place of the Navier-Stokes \mathbf{Q} tensor in (2) and (3).

4. Results and Comparisons

4.1. Shu-Osher Shock Wave

As a first point of comparison between the CSW-Q and Hyper-Q models, we consider the Shu-Osher problem, a canonical model of a one-dimensional shock-turbulence interaction [34]. The nondimensional initial conditions are: $\rho = 3.857143$, $p = 10.33333$ and $u = 2.629369$ for $x < -4$, and $\rho = 1 + 0.2\sin(5x)$, $p = 1$ and $u = 0$ for $x \geq -4$, with $\gamma = 1.4$. As the shock propagates into the sinusoidal density field, it leaves a steeply oscillating flow in the post-shock region.

Figure 3 shows the results of the two artificial viscosity models compared to the converged solution. In one dimension, the CSW-Q and Hyper-Q models capture shocks in virtually identical fashion. They also reproduce the post-shock oscillations with similar fidelity. In one dimension, grid cells collapse to edges, which causes the cell- and edge-centered schemes to behave similarly. In this and other one-dimensional shock problems (not shown),

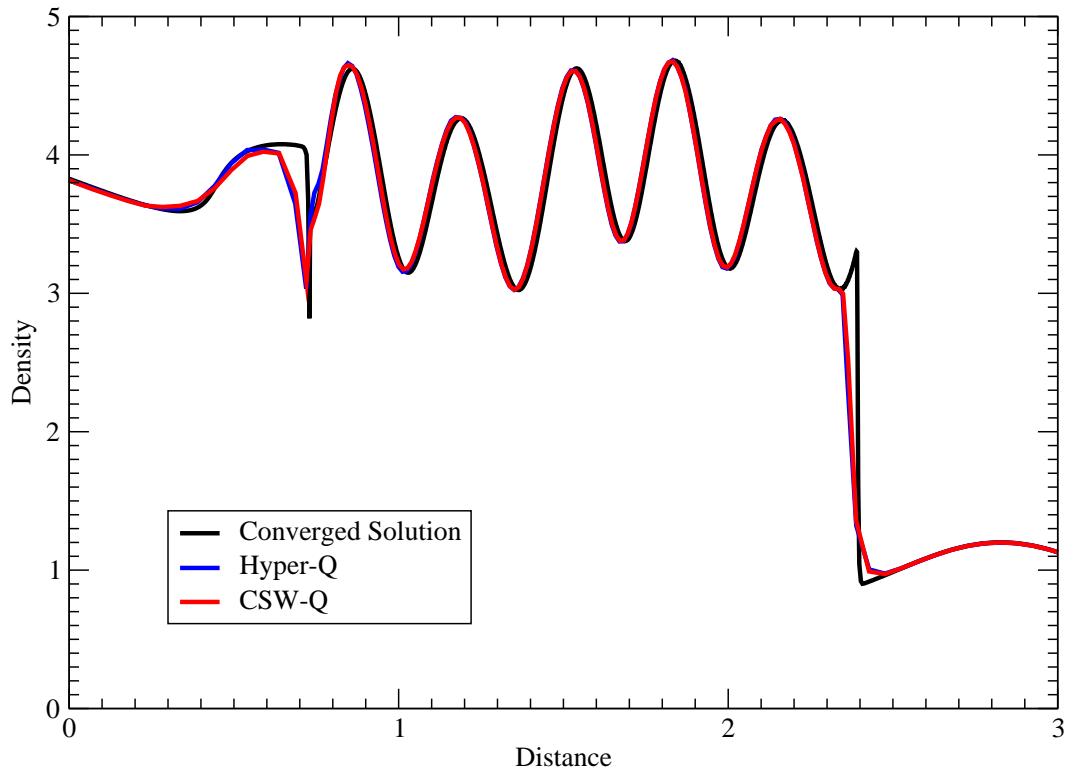


Figure 3: Density for Shu-Osher problem at $t = 1.8$. The Hyper-Q and CSW-Q results were obtained from Lagrangian simulations using an initial grid resolution of $\Delta x = 0.05$.

the shock profiles are very similar, with about 3 zones inside the shock. Larger/smaller values of C_β lead to thicker/thinner shocks. It has previously been demonstrated that for a given value of C_β , the shock is spread over a fixed number of grid points, regardless of shock strength [13, 16].

4.2. Noh Implosion

The Noh problem tests a model’s ability to distinguish shocks from uniform adiabatic compression. It consists of a infinite-strength shock propagating outward into a converging flow [35, 36]. It is described nondimensionally by:

$$\rho, u_r, e = \begin{cases} [(\gamma + 1)/(\gamma - 1)]^d, 0, 1/2 & \text{if } r < r_s \\ (1 + t/r)^{(d-1)}, -1, 0 & \text{if } r \geq r_s \end{cases}, \quad (23)$$

$$r_s = t(\gamma - 1)/2, \quad (24)$$

where $d = 1, 2, 3$ is the dimension of the problem (planar, cylindrical or spherical), u_r is radial (or x) velocity and r_s is the radial (or x) position of the shock. We ran the problem in cylindrical (RZ) and Cartesian (XY) coordinates, with the latter performed both with and without symmetry boundaries. The initial grid for the full XY case (without symmetry boundaries) is displayed in Fig. 4. This type of “butterfly” mesh is commonly used for cylindrical and spherical problems in order to avoid the singularity at the origin.

The simulations were run in a purely Lagrangian mode; i.e., $\hat{\mathbf{u}} = \mathbf{u}$ with no remapping. The density fields at $t = 0.6$ are compared in Fig. 5. The post-shock densities for the RZ (top) and XY (middle and bottom) cases should be 64 and 16, respectively. The maximum Hyper-Q densities are reasonably close to the exact values; however, the maximum CSW-Q densities are much higher; i.e., 94.4 (before crashing), 29.6 and 31.0 for the top, middle and bottom cases, respectively. Whereas, the Hyper-Q model preserves circular symmetry reasonably well, CSW-Q generates enormous spikes in the cardinal directions and minor spikes where the inner square mesh meets the outer circular mesh. The CSW-Q spikes are exacerbated by the model’s limiter, which turns off the artificial viscosity in regions of uniform compression.

The lower density near the origin (in all cases) is a manifestation of the well-known “wall heating” problem [37]. This can be solved by adding an artificial conductivity; however, that is beyond the scope of this paper. Excessive heating near the origin results in an increased sound speed which causes the shock to run somewhat fast (it should be at a radius of 0.2 at

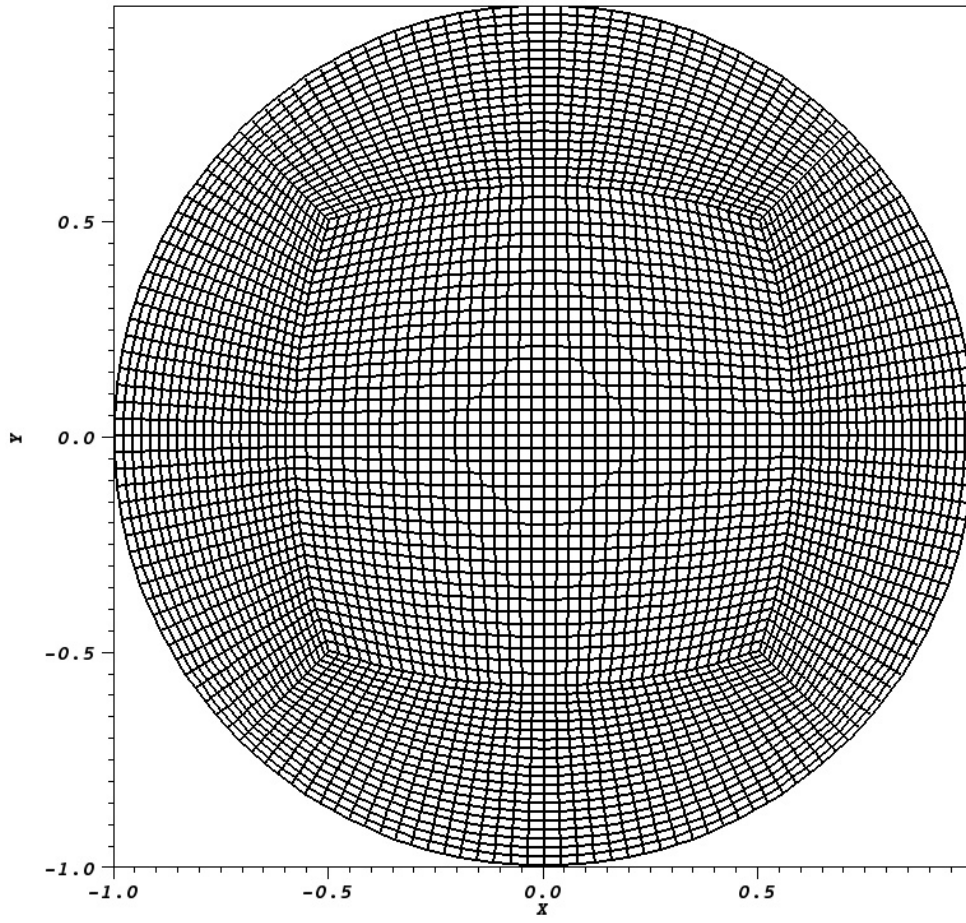


Figure 4: Initial grid for XY Noh problem.

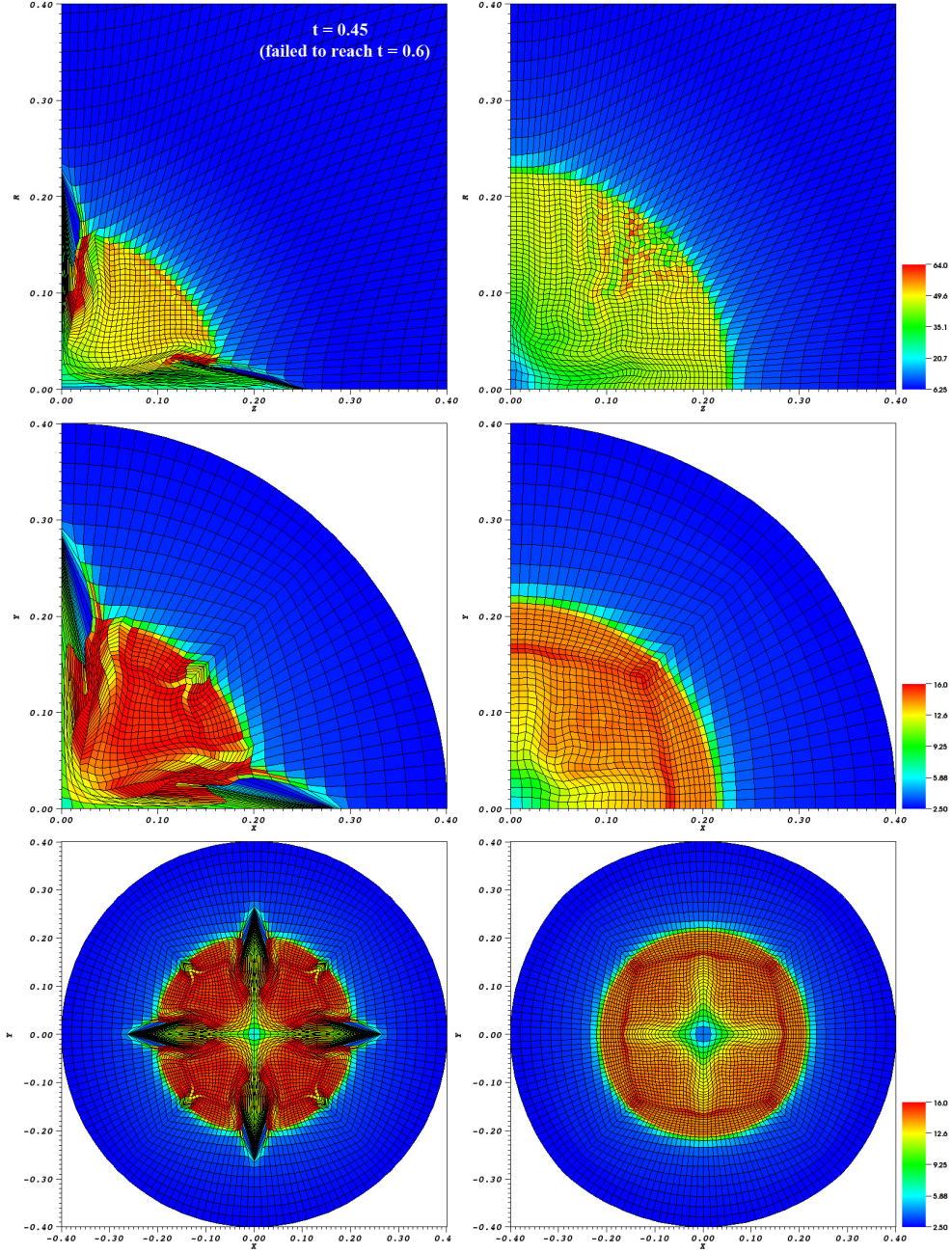


Figure 5: Density for the Noh problem at $t = 0.6$. The CSW-Q results are on the left and the Hyper-Q results are on the right. The top simulations were performed on a square mesh in RZ coordinates ($d = 3$). The middle simulations were performed in XY coordinates ($d = 2$) with symmetry boundaries. The bottom simulations were performed in XY coordinates without symmetry boundaries.

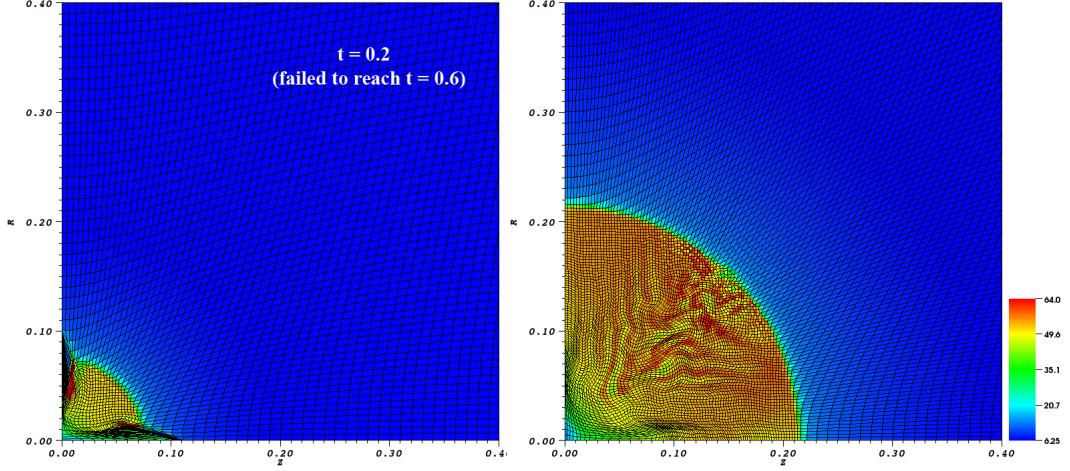


Figure 6: Density for the RZ Noh problem at $t = 0.6$ using double the resolution as in Fig. 5. The CSW-Q results are on the left and the Hyper-Q results are on the right. The CSW-Q model generates densities as large as 92.5 before crashing.

the times shown). By doubling the resolution (see Fig. 6) the error in shock location is reduced by half, indicating first-order convergence. The CSW-Q model fails sooner when the grid is refined.

4.3. Sedov Blast Wave

Whereas, the Noh problem is purely compressive, the Sedov-Taylor-von Neumann blast wave [38, 39, 40] is strongly expansive. The nondimensional initial conditions are: $\rho = 1$, $\mathbf{u} = 0$ and $e = e_o \delta(r)$ (where r is radius), and we set $e_o = 1$ and $\gamma = 7/5$. The location of the shock front is given by

$$r_s(t) = (e_o/\alpha)^{1/(2+d)} t^{2/(2+d)}, \quad (25)$$

where $d = 1, 2, 3$ is the dimension of the problem and α is a parameter which depends on the solution and can be obtained iteratively [38]. A challenging aspect of this problem is that the blast wave leaves behind a vacuum at the origin.

Once again, we ran the problem in Lagrangian fashion on a square RZ mesh, a symmetric XY mesh and a full XY mesh. Results for the two models are presented in Fig. 7. The Hyper-Q model preserves spherical/cylindrical symmetry, whereas CSW-Q once again produces spikes along the axes, similar to the Noh results.

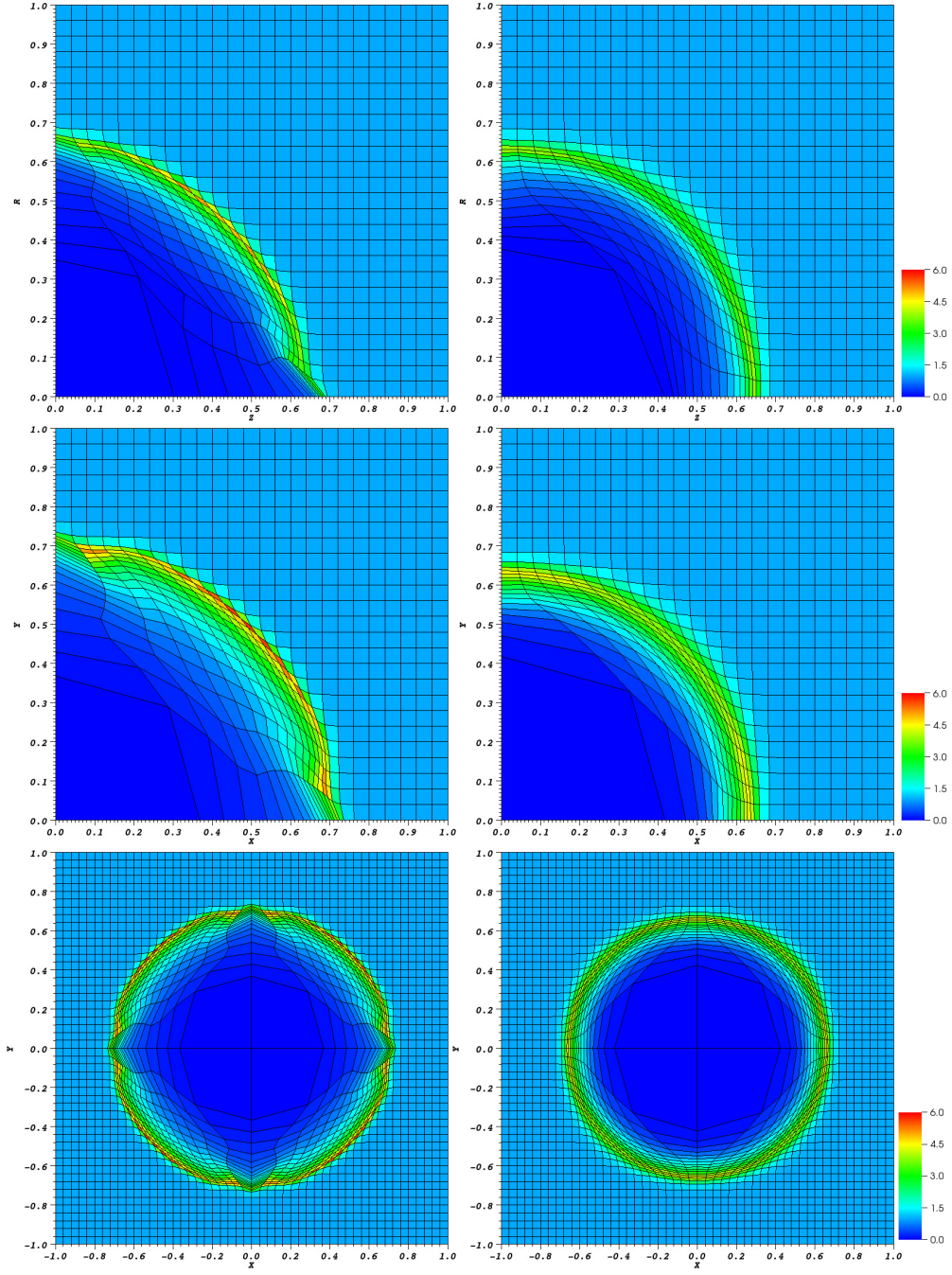


Figure 7: Density for Sedov blast wave. The CSW-Q results are on the left and the Hyper-Q results are on the right. Top: solution in cylindrical (RZ) coordinates ($d=3$) at $t = 0.3$. Middle: solution in Cartesian (XY) coordinates ($d=2$) at $t = 0.5$ using symmetry boundaries. Bottom: solution in XY coordinates ($d=2$) at $t = 0.5$ on a full 360-degree grid.

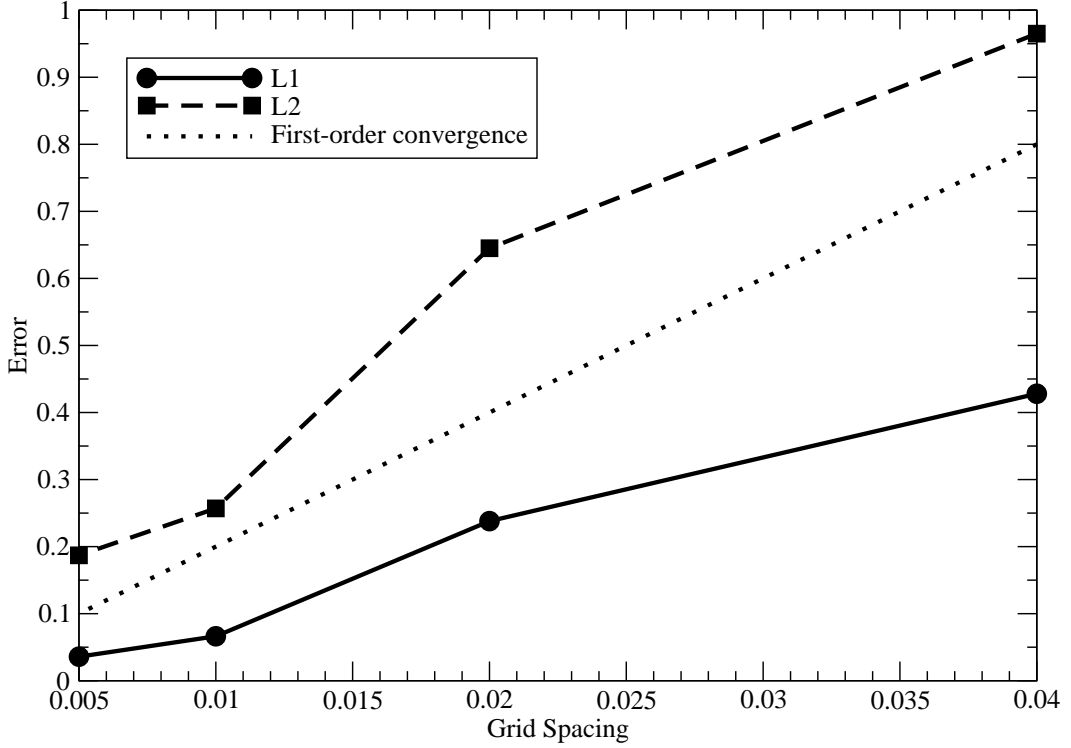


Figure 8: Convergence of Hyper-Q model on exact solution for Sedov blast wave at $t = 0.3$ using $e_0 = 4.48333289847$. The solid and dashed lines are the L1 and L2 error norms of the simulation as functions of initial grid resolution. The dotted line corresponds to first-order convergence

To ensure that the Hyper-Q model converges to the exact solution for a strong source, we performed a refinement study with $e_0 = 4.48333289847$. With this initial energy, the analytical solution places the shock at $r = 0.8$ at $t = 0.3$. Figure 8 shows approximately first-order convergence for the scheme.

4.4. Saltzman Piston

In order to test the robustness of the models for Lagrangian simulations on nonideal grids, we consider the Saltzman piston problem, which consists of an infinite-strength shockwave driven by a piston. A nondimensional box of width 1.0 and height 0.1 contains a $\gamma = 5/3$ gas with $\rho = 1$ and $e = 0$. At $t = 0$, the left wall begins moving to the right at a speed of 1.0 (while the right wall remains fixed). The initial grid is distorted in order to test

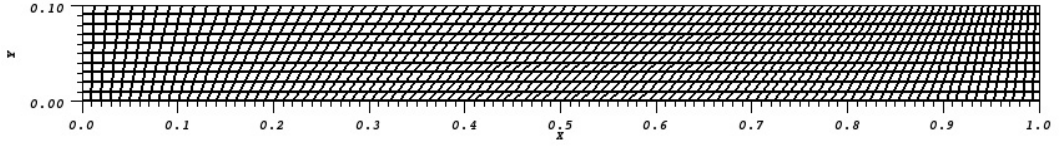


Figure 9: Initial grid for Saltzman piston problem.

the models' ability to preserve the 1D solution on a nonideal mesh, which is shown (at time zero) in Fig. 9. Prior to shock reflection, this problem is identical to the 1D Noh problem with a change of reference frame. The shock hits the right wall at $t = 0.75$, rebounds off the piston at $t = 0.9$ and impacts the right wall again at $t = 0.95$. The density behind the shock prior to the first, second and third bounces is 4, 10 and 20, respectively.

In Fig. 10, the two models are compared just before each bounce. As the shock propagates through the distorted grid, it generates spurious vorticity. This grid-seeded vorticity is damped to different degrees by the artificial viscosity models. For the employed model coefficients, the CSW-Q model damps vorticity more strongly than the Hyper-Q model.

A smoother grid for Hyper-Q could be obtained with a larger C_μ ; however, this would come at the expense of increased dissipation in other problems (to be discussed). It is often possible to achieve improved results on one-dimensional flows such as this by increasing the artificial damping. However, this is not necessarily desirable, since increased dissipation can degrade results on vortical flows. A better option here would be to enable grid remapping before the grid becoming so grossly distorted. The primary objective of this problem is to demonstrate that both models enable Lagrangian simulations to run robustly, even when the grid becomes severely distorted.

4.5. Taylor-Green Vortex

Thus far, all of the test cases have involved one-dimensional irrotational flows, which have primarily exercised β^* . In order to test the efficacy of μ^* at capturing turbulence, we need a flow which activates all components of the **Q** tensor in three dimensions. Therefore, as a final point of comparison, we consider the Taylor-Green vortex [41], which is well-suited for testing artificial shear viscosity. As the vortex stretches and bends in three dimensions, kinetic energy cascades to smaller scales. Stretching and bending of vortex lines constitute key energy transfer mechanisms in turbulent flows.

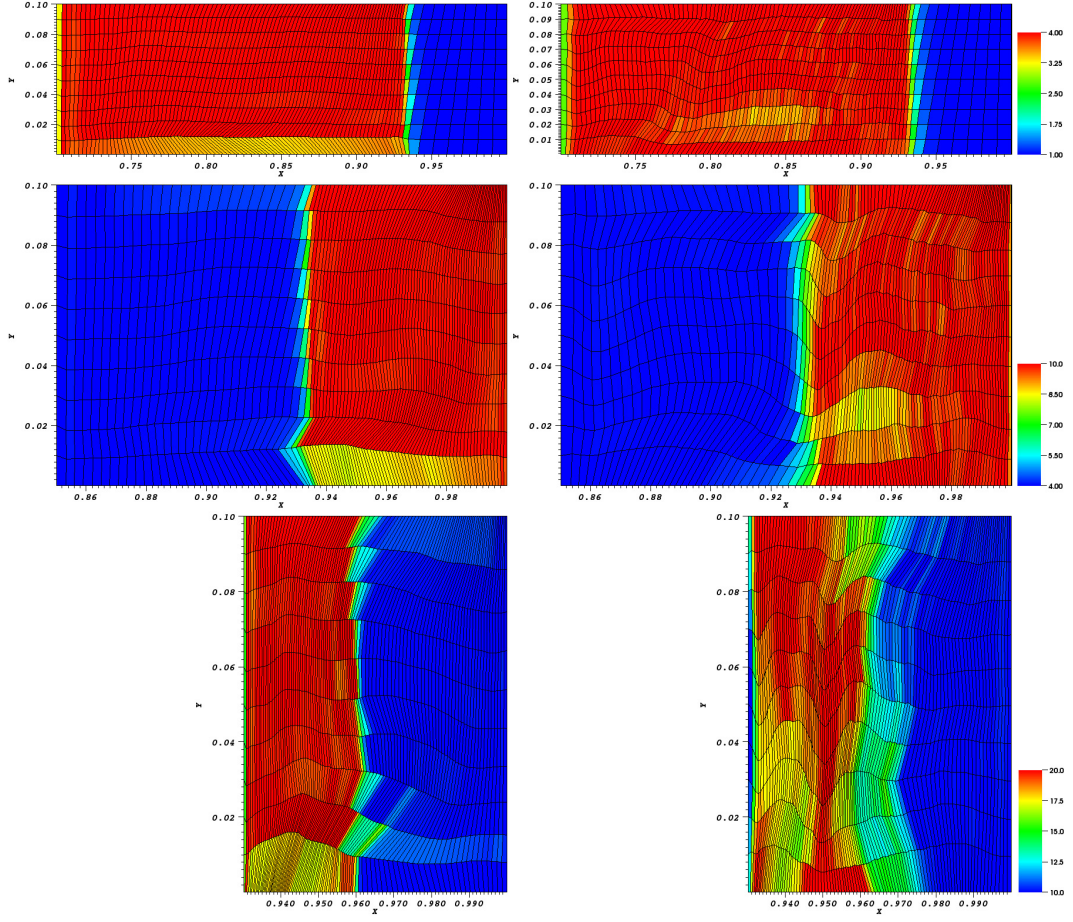


Figure 10: Density for Saltzman piston at $t = 0.7$ (top), $t = 0.85$, (middle) and $t = 0.93$ (bottom). The CSW-Q solution is on the left and the Hyper-Q solution is on the right.

The initial conditions for the problem are:

$$\begin{aligned}
\rho &= 1 , \\
u &= \sin(x) \cos(y) \cos(z) , \\
v &= -\cos(x) \sin(y) \cos(z) , \\
w &= 0 , \\
p &= p_o + [\cos(2x) + \cos(2y)][\cos(2z) + 2]/16 , \\
\gamma &= 5/3 ,
\end{aligned} \tag{26}$$

where the pressure corresponds to the incompressible-flow solution. The arbitrary constant p_o is set to 100 to make the Mach number very low, such that the incompressible solution, at early time, can be used for comparison [42]. The computational domain is a triply-symmetric π^3 box on a 32^3 grid. For both models, we ran the code in Eulerian mode ($\hat{\mathbf{u}} = 0$), ALE mode ($0 \leq \hat{\mathbf{u}} \leq \mathbf{u}$) and Lagrangian mode ($\hat{\mathbf{u}} = \mathbf{u}$), in order to assess the interplay between the remapping algorithm and the artificial viscosity. Results for each case are illustrated in Fig. 11. This problem requires fairly aggressive remapping in order to run very far; hence, the Eulerian and ALE results appear similar. The Lagrangian simulations were run up to $t = 2$, shortly after which they both crashed, due to severe mesh distortion.

As the flow evolves, vorticity becomes concentrated at smaller and smaller scales, which makes the artificial viscosity become increasingly active. Figure 12 shows the time dependence of normalized total enstrophy, defined as $\Omega(t)/\Omega(0)$, where

$$\Omega(t) \equiv \frac{1}{2} \int_0^\pi \int_0^\pi \int_0^\pi \boldsymbol{\omega} \cdot \boldsymbol{\omega} \, dx \, dy \, dz . \tag{27}$$

Analysis based on Padé approximants and the behavior of the analyticity strip, predicts $\Omega(t)$ will become far too large (possibly infinite) to capture on a such a coarse grid [43]; nevertheless, the ability of a scheme to track the analytical enstrophy curve, as well as the maximum enstrophy that a scheme is able to generate, are stringent tests of resolving power. The results indicate that the Hyper-Q model is much better at capturing small-scale vorticity than CSW-Q; i.e., Hyper-Q is less dissipative than CSW-Q in all three modes of operation. Furthermore, CSW-Q exhibits some sensitivity to the remapping strategy (Eulerian versus ALE), whereas Hyper-Q does not. As a side note, it is readily apparent that the remapping algorithm in the Eulerian and ALE cases is very strongly dissipative.

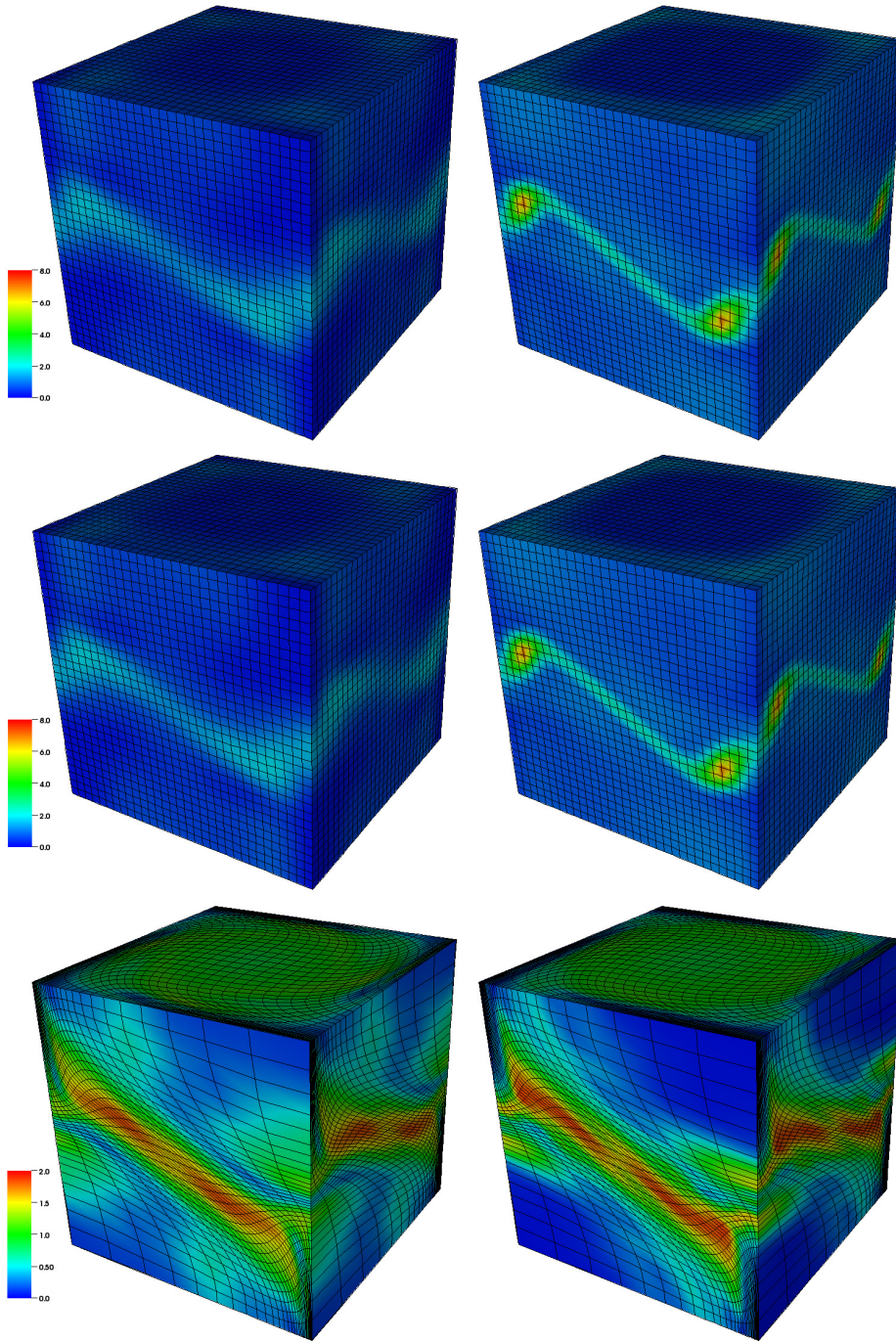


Figure 11: Vorticity for the Taylor-Green vortex. CSW-Q is on the left and Hyper-Q is on the right. The top images are at $t = 5$ running in Eulerian mode. The middle images are at $t = 5$ running in ALE mode. The bottom images are at $t = 2$ running in Lagrangian mode.

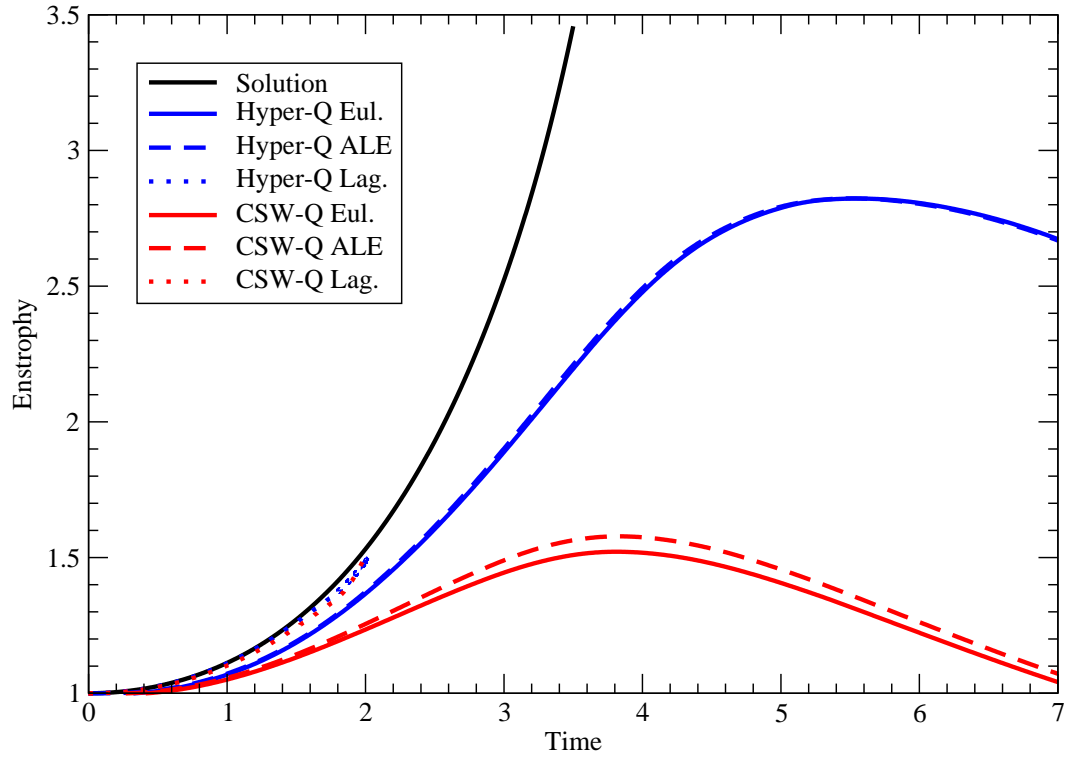


Figure 12: Normalized enstrophy versus time for the Taylor-Green vortex. Simulations were performed on a π^3 symmetric box with 32^3 grid points.

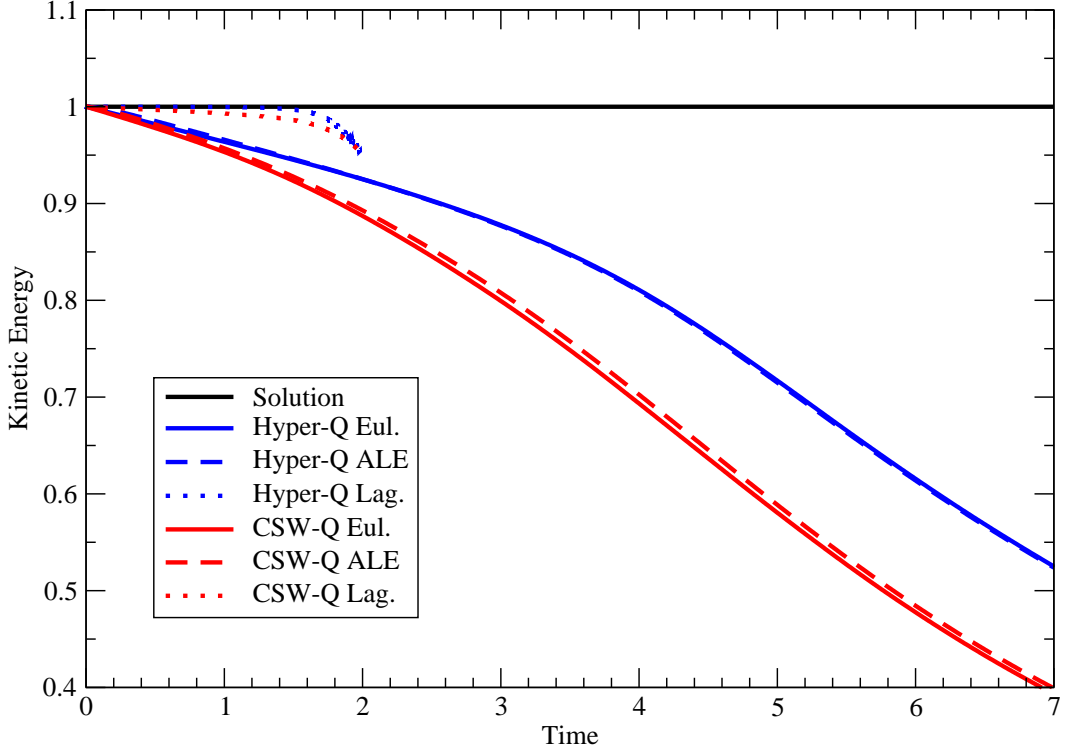


Figure 13: Normalized kinetic energy versus time for the Taylor-Green vortex.

Another means of quantifying numerical dissipation in this flow is to examine the evolution of normalized kinetic energy, i.e., $K(t)/K(0)$, where

$$K(t) = \frac{1}{2} \int_0^\pi \int_0^\pi \int_0^\pi \rho \mathbf{u} \cdot \mathbf{u} \, dx \, dy \, dz .$$

This is plotted in Figure 13 for each of the simulations. Since the flow is very nearly incompressible, kinetic energy should be conserved. Once again we see that CSW-Q is more dissipative in all three cases than Hyper-Q. The CSW-Q model also generates some difference between the Eulerian and ALE results; whereas, Hyper-Q appears insensitive to the remapping algorithm. The Lagrangian simulations preserve kinetic energy much better than the Eulerian and ALE simulations; in fact, the remapping algorithm causes severe loss of kinetic energy from the very beginning when only large-scale motions are present and the flow is very smooth. This is a very serious problem; however, the remapping algorithm is beyond the scope of our current investigations.

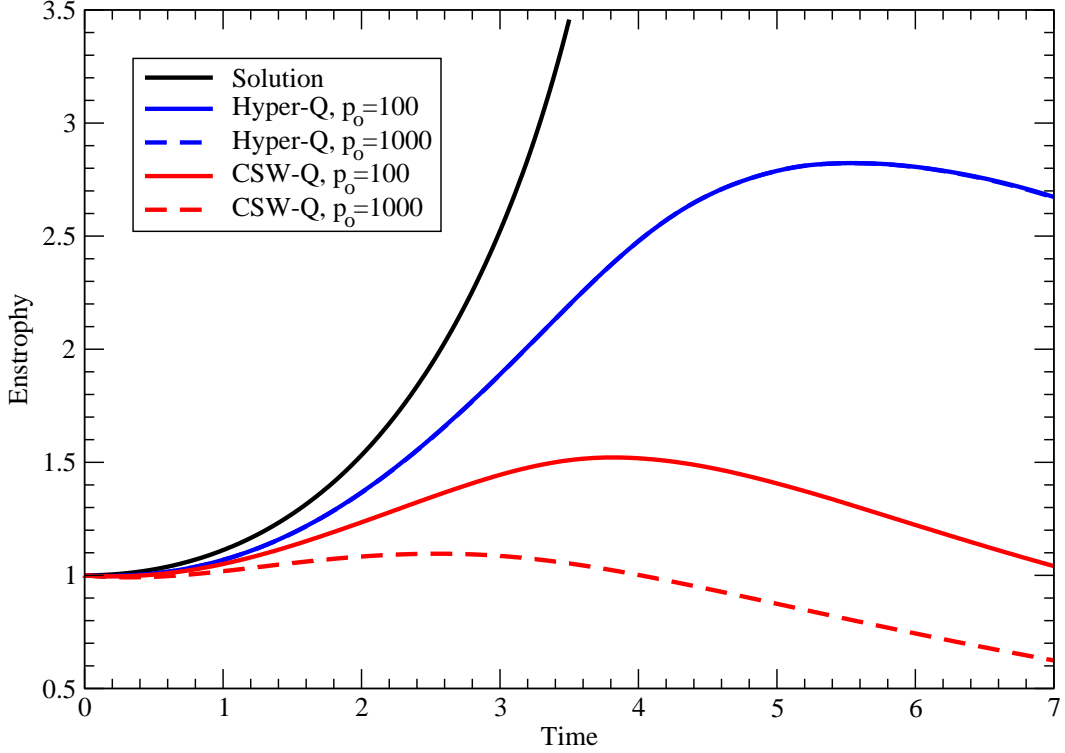


Figure 14: Normalized enstrophy versus time for the Taylor-Green vortex. Simulations were run in Eulerian mode with different background pressures. The Hyper-Q curves lie on top of one another.

The excessive dissipation of vorticity and kinetic energy in the CSW-Q model is partly due to its dependence on sound speed. To illustrate this point, we repeated the Eulerian calculations with $p_o = 1000$ (recall that sound speed is $\sqrt{\gamma p/\rho}$). In the incompressible limit, the governing equations depend only on the pressure gradient, not the pressure itself; hence, the simulation results should not be sensitive to p_o (at these very low Mach numbers). Figure 14 shows the enstrophy results for the two models running at the different background pressures. The Hyper-Q model is independent of the background pressure/Mach number; whereas, the CSW-Q model becomes increasingly dissipative as the Mach number goes to zero. The sound speed scaling of the linear term in CSW-Q causes the artificial viscosity to blow up as the Mach number goes to zero. This unphysical behavior is highly problematic for turbulence calculations. Artificial viscosity should not depend on sound

speed.

5. Conclusions

The Hyper-Q model performs similarly to the CSW-Q model on one-dimensional shock problems, with each model spreading shocks over about 3 grid cells. In higher dimensions, the Hyper-Q model better preserves cylindrical/spherical symmetry on the Noh and Sedov problems. The CSW-Q model dissipates vorticity much more strongly than the Hyper-Q model. The strongly dissipative behavior of CSW-Q enables it to produce very robust results on the Saltzman piston; however, it leads to very poor results on the Taylor-Green vortex.

The new Hyper-Q model employs the Navier-Stokes form of the viscous stress tensor, including the bulk-viscosity term. This enables it to capture both shocks and turbulence in a frame-independent manner. By basing the bulk viscosity term on the curvature (Laplacian) of the divergence, rather than on the divergence itself, shocks are distinguished from uniform compression without the need for detectors, limiters or switches. By modeling the shear viscosity on the curvature of the strain-rate magnitude and grid-length parameter, Lagrangian calculations are made more robust and vorticity is captured on the grid without excessive dissipation.

Finally, unlike most other artificial-viscosity models for shock-capturing, the Hyper-Q model is compatible with very low Mach number flow, since it does not depend on sound speed. We believe the Hyper-Q model will prove useful in ALE codes using either structured or unstructured meshes.

Acknowledgements

This work was performed under the auspices of the U.S. Department of Energy by Lawrence Livermore National Laboratory under Contract DE-AC52-07NA27344.

References

- [1] J. von Neumann, R. D. Richtmyer, A method for the numerical calculations of hydrodynamical shocks, *J. Appl. Phys.* 21 (1950) 232–237.
- [2] W. D. Schulz, Two-dimensional Lagrangian hydrodynamic difference schemes, *Methods Comput. Phys.* 3 (1964) 1.

- [3] M. L. Wilkins, Use of artificial viscosity in multidimensional shock wave problems, *J. Comput. Phys.* 36 (1980) 281.
- [4] A. Jameson, W. Schmidt, E. Turkel, Numerical simulation of the Euler equations by finite volume methods using Runge-Kutta time stepping schemes, AIAA paper 81-1259, AIAA 5th Computations Fluid Dynamics Conference, 1981.
- [5] E. Tadmor, Convergence of spectral methods for nonlinear conservation laws, *SIAM J. Numer. Anal.* 26 (1989) 30.
- [6] C. K. W. Tam, J. W. Webb, Z. Dong, A study of the short wave components in computational aeroacoustics, *J. Comput. Acoustics* 1 (1993) 1–30.
- [7] A. Misra, D. I. Pullin, A vortex-based subgrid stress model for large-eddy simulation, *Phys. Fluids* 9 (1997) 2443–2454.
- [8] G. Dantinne, H. Jeanmart, G. S. Winckelmans, V. Legat, D. Carati, Hyperviscosity and vorticity-based models for subgrid scale modeling, *Applied Scientific Research* 59 (1998) 409–420.
- [9] G.-S. Karamanos, G. E. Karniadakis, A spectral vanishing viscosity method for large-eddy simulations, *J. Comput. Phys.* 163 (2000) 22–50.
- [10] C. L. M. H. Navier, *Mémoire sur les lois du mouvement des fluides*, *Mémoires de l’Academie des Sciences* 6 (1823) 389–416.
- [11] G. G. Stokes, On the theories of the internal friction in fluids in motion, and of the equilibrium and motion of elastic solids, *Transactions of the Cambridge Philosophical Society* 8 (1845) 287–342.
- [12] E. J. Caramana, M. J. Shashkov, P. P. Whalen, Formulations of artificial viscosity for multi-dimensional shock wave computations, *J. Comput. Phys.* 144 (1998) 70–97.
- [13] A. W. Cook, W. H. Cabot, A high-wavenumber viscosity for high-resolution numerical methods, *J. Comput. Phys.* 195 (2004) 594–601.
- [14] A. W. Cook, W. H. Cabot, Hyperviscosity for shock-turbulence interactions, *J. Comput. Phys.* 203 (2005) 379–385.

- [15] A. W. Cook, Artificial fluid properties for large-eddy simulation of compressible turbulent mixing, *Phys. Fluids* 19 (2007) 055103.
- [16] B. Fiorina, S. K. Lele, An artificial nonlinear diffusivity method for supersonic reacting flows with shocks 222 (2007) 246–264.
- [17] S. Kawai, S. K. Lele, Localized artificial diffusivity scheme for discontinuity capturing on curvilinear meshes, *J. Comput. Phys.* 227 (2008) 9498–9526.
- [18] A. W. Cook, Enthalpy diffusion in multicomponent flows, *Phys. Fluids* 21 (2009) 055109.
- [19] A. Mani, J. Larsson, P. Moin, Suitability of artificial bulk viscosity for large-eddy simulation of turbulent flows with shocks, *J. Comput. Phys.* 228 (2009) 7368–7374.
- [20] G. Lacaze, B. Cuenot, T. Poinso, M. Oschwald, Large eddy simulation of laser ignition and compressible reacting flow in a rocket-like configuration, *Combust. Flame* 156 (2009) 1166–1180.
- [21] A. Roux, L. Y. M. Gicquel, S. Reichstadt, N. Bertier, G. Staffelbach, F. Vuillot, T. J. Poinso, Analysis of unsteady reacting flows and impact of chemistry description in large eddy simulations of side-dump ramjet combustors, *Combust. Flame* 157 (2010) 176–191.
- [22] S. K. Shankar, S. Kawai, S. K. Lele, Two-dimensional viscous flow simulation of a shock accelerated heavy gas cylinder, *Phys. Fluids* 23 (2011) 024102.
- [23] A. Bhagatwala, S. K. Lele, Interaction of a Taylor blast wave with isotropic turbulence, *Phys. Fluids* 23 (2011) 035103.
- [24] B. Enaux, V. Granet, O. Vermorel, C. Lacour, L. Thobois, V. Dugué, T. Poinso, Large eddy simulation of a motored single-cylinder piston engine: Numerical strategies and validation, *Flow, Turbulence and Combustion* 86 (2011) 153–177.
- [25] S. Pirozzoli, Numerical methods for high-speed flows, *Annu. Rev. Fluid Mech.* 43 (2011) 163–194.

- [26] A. N. Kolmogoroff, The local structure of turbulence on incompressible viscous fluid for very large Reynolds numbers, *C. R. Acad. Sci., U.S.S.R.* 30 (1941) 301.
- [27] E. J. Caramana, D. E. Burton, M. J. Shashkov, P. P. Whalen, The construction of compatible hydrodynamics algorithms utilizing conservation of total energy, *J. Comput. Phys.* 146 (1998) 227–262.
- [28] E. J. Caramana, C. L. Rousculp, D. E. Burton, A compatible, energy and symmetry preserving lagrangian hydrodynamics algorithm in three-dimensional cartesian geometry, *J. Comput. Phys.* 157 (2000) 89–119.
- [29] D. Flanagan, T. Belytschko, A uniform strain hexahedron and quadrilateral with orthogonal hourglass control, *Int. J. Numer. Methods Eng.* 17 (1981) 679–706.
- [30] L. G. Margolin, J. J. Pyun, A Method for Treating Hourglass Patterns, Technical Report LA-UR–87-439, Los Alamos National Laboratory, 1987.
- [31] E. Caramana, M. Shashkov, Elimination of artificial grid distortion and hourglass-type motions by means of lagrangian subzonal masses and pressures, *J. Comput. Phys.* 142 (1998) 521–561.
- [32] J. Campbell, M. J. Shashkov, A tensor artificial viscosity using a mimetic finite difference algorithm, *J. Comput. Phys.* 172 (2001) 739–765.
- [33] V. F. Kuropatenko, in: N. N. Janenko (Ed.), *Difference Methods for Solutions of Problems of Mathematical Physics*, 1, Amer. Math. Soc., Providence, 1967, p. 116.
- [34] C.-W. Shu, S. J. Osher, Efficient implementation of essentially non-oscillatory shock capturing schemes II, *J. Comput. Phys.* 83 (1989) 32–78.
- [35] W. F. Noh, Errors for calculations of strong shocks using an artificial viscosity and an artificial heat flux, *J. Comput. Phys.* 72 (1987) 78–120.
- [36] M. Gehmeyr, B. Cheng, D. Mihalas, Noh’s constant-velocity shock problem revisited, *Shock Waves* 7 (1997) 255–274.

- [37] W. J. Rider, Revisiting wall heating, *J. Comput. Phys.* 162 (2000) 395–410.
- [38] L. I. Sedov, *Similarity and Dimensional methods in Mechanics*, Fourth Ed., Academic Press, New York, 1959.
- [39] G. I. Taylor, The formation of a blast wave by a very intense explosion: I, ii, *Proc. Roy. Soc. London, Ser. A* 201 (1950) 155–175.
- [40] L. D. Landau, E. M. Lifshitz, *Fluid Mechanics*, Addison-Wesley, Reading, Mass., 1959.
- [41] G. I. Taylor, A. E. Green, Mechanism of the production of small eddies from large ones, *Proc. Roy. Soc. A* 158 (1937) 499–521.
- [42] M. E. Brachet, D. I. Meiron, S. A. Orszag, B. G. Nickel, R. H. Morf, U. Frisch, Small-scale structure of the Taylor-Green vortex, *J. Fluid Mech.* 130 (1983) 411–452.
- [43] R. H. Morf, S. A. Orszag, U. Frisch, Spontaneous singularity in three-dimensional, inviscid, incompressible flow, *Phys. Rev. Lett.* 44 (1980) 572–575.